Power Characteristics in GMAW: Experimental and Numerical Investigation

Arc length proves to be a significant controlling factor for energy passing through the arc

BY P. G. JÖNSSON, J. SZEKELY, R. B. MADIGAN AND T. P. QUINN

ABSTRACT. The voltage and power distributions in gas metal arc welding (GMAW) were studied both experimentally and numerically. The principal voltage drop takes place in the arc, which also constitutes the dominant power contribution. Within the arc, the dominating voltage contributions are from the arc column and the cathode fall, while the anode fall and the electrode regions are less significant. The power input to the arc column increases with both increasing current and increasing arc length. These results indicate that it is critical to control the arc length in order to control the power input to the system.

Introduction

In gas metal arc welding (GMAW), a consumable electrode is melted, forming metal droplets that are then transferred to the workpiece where they solidify. This transformation affects the final shape and quality of the weld (Ref. 1). In order to control this transfer process, it is necessary to understand the influence of arc characteristics such as power, voltage, and temperature on droplet formation and detachment, and the general nature of the arc-weld pool interactions.

Eagar (Ref. 2) concluded that the temperature of the welding arc does not have a primary effect on the arc welding process. This conclusion was based on the work by Cobine and Burger (Ref. 3) and Quigley, *et al.* (Ref. 4), who showed that the major part of the energy transferred to the anode from the welding arc is carried by the electric current, while convection and radiation from the plasma gases are responsible for only a minor part of the energy transferred. These findings show the importance of studying the electrical characteristics in the GMAW system. Some work has been done to address the voltage-current (U-I) relationship for GMAW. Jackson, for example, reported data on the U-I characteristics for GMAW of steel for various shielding gases (Ref. 5). Also, Halmøy derived the arc voltage as a function of both current and arc length (Refs. 6, 7). In that study, the arc voltage was defined as the welding voltage minus the voltage in the electrode extension.

KEY WORDS

Power Characteristic
GMAW
Voltage Distribution
Power Distribution
Experimental Invest.
Numeric Investigation
Arc Length
Power Input
Theoretical Models
Arc Column

The purpose of this article is to describe our study of the power characteristics in GMAW of mild steel. In doing so, we first had to study the voltage characteristics of the system. The first part of the article reviews the literature and describes our theoretical modeling work. Then we present the experimental procedure, and evaluate the voltage contributions in the different parts of the GMAW system, and the power characteristics in the arc.

Background

The GMAW arc region for a conventional reverse polarity arc consists of the following main components, as shown in Fig. 1: contact tube, consumable electrode, anode fall region, arc column, cathode fall region, and workpiece (weld pool). The distribution of electric potential between the contact tube and the workpiece can be divided into the following separate contributions to voltage drops: due to the contact resistance between the contact tube and the consumable electrode (U_{cont}), consumable electrode (U_{elec}), anode fall region (U_{an}), arc column (U_{col}), and cathode fall region (U_{cat}).

Below, we briefly discuss previous work dealing with these individual arc components. For cases where no information is available for GMAW systems, studies dealing with other arcs will be included for completeness. We also present an equation for evaluating power

P. G. JÖNSSON is with MEFOS, Luleå, Sweden. J. SZEKELY is with Dept. of Materials Science and Engineering, MIT, Cambridge, Mass. R. B. MADIGAN and T. P. QUINN are with Materials Reliability Division, NIST, Boulder, Colo.

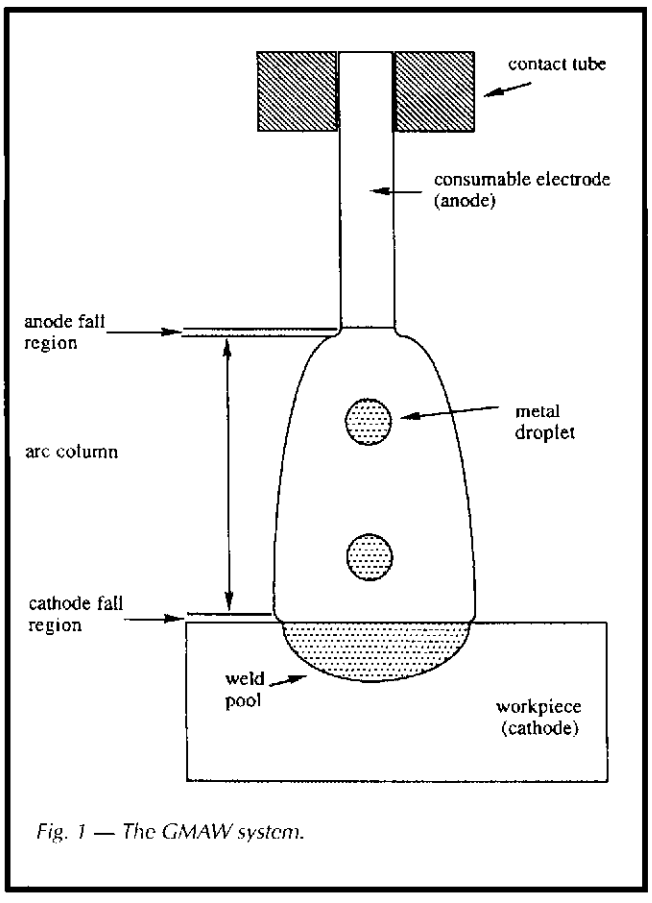

Fig. 1 — The GMAW system.

characteristics and discuss previous studies dealing with arc power and arc radiation.

Voltage Characteristics

U_{cont}

The voltage drop due to the contact resistance between a contact tube and a stainless steel electrode was experimentally determined by Wassink and van den Heuvel (Ref. 8). A voltage drop of 0.3 V to 0.6 V was measured for currents of 100 to 250 A, arc lengths of 6 to 10 mm (0.24 to 0.4 in.), and electrode extensions of 27.5 to 37.5 mm (1.1 to 1.5 in.).

U_{elec}

Halmøy (Ref. 7) presented an expression for the total voltage in the consumable electrode U_{elec} in GMAW given as

$$U_{elec} = \frac{H_m v_w}{J} - \varphi \quad (1)$$

where H_m is an experimental constant representing the total heat input per unit volume of wire necessary to melt and detach the droplets, v_w is the wire feed speed, J is the current density, and φ is the work function of the electrode material. The voltage drop in a consumable steel electrode has also been studied by Waszink and van den Heuvel (Ref. 8). The voltage drop was 4.0 V to 4.5 V for a current of 150 A, a wire speed of 0.074 m/s (175 in./min), and an electrode extension of 37.5 mm.

U_{an}

The anode fall represents a layer in which local thermal equilibrium does not exist (non-LTE). For gas tungsten arcs the temperature of the heavy particles (ions, atoms) rapidly approaches the temperature of the anode, while the electron temperature remains high, to maintain a conducting path, even close to the anode surface (Ref. 9). The maximum thickness of the anode fall region, to which these nonequilibrium effects are confined, has experimentally been determined as 0.05 to 0.1 mm for carbon arcs (Refs. 10, 11).

The anode fall voltage for metals in an argon atmosphere has been measured and estimated to range from 1 to 11 V for arc lengths of 1 to 10 mm and currents of 50 to 500 A (Refs. 12–15). In these studies, U_{an} decreased as the current or the temperature near the anode increased with a reduction in the arc length (Refs. 12, 15). In another study, the anode fall voltage decreased with a decreasing thermal conductivity of the base metal (Ref. 16), and finally, some analyses even predicted the anode fall voltage to be negative (Refs. 17, 18). All this work was carried out in GTAW systems. As far as we know, no similar work pertaining to GMAW systems has been reported in the literature.

U_{cat}

Similar to the anode region, the cathode fall region also represents an area where non-LTE exists. For gas tungsten arcs, the temperatures of the heavy particles approach the temperature of the cathode surface, while the electron temperatures remain higher. The electrons are responsible for providing electric conductivity (Refs. 19–21). The maximum thickness of the cathode boundary layer has been experimentally estimated as 0.1 mm for thermionic cathodes found in GTAW (Ref. 10).

The physics of the cathode fall region in GMAW of iron-based alloys is not well understood. Guile lists iron as an element for which it is not clear whether cathodic emission of electrons is thermionic or nonthermionic (Ref. 22). However, several observations indicate that iron behaves more nonthermionic than thermionic. First, Essers and Walter found that the calculated value of the current density, as a result of thermionic emission, is very low (Ref. 23). Second, calculated values of the current density, as a result of thermionic emission, have shown good agreement only with experimental data on materials with boiling points of at least 4000 K (Ref. 16) The boiling point of iron is approximately 3273 K. Finally, a mobile cathode behavior, similar to what is usually observed for nonthermionic cathodes such as aluminum (Ref. 24), is also observed in GMAW of steel (Ref. 25).

Though there has not been extensive research on the voltage drop in the cathode region (U_{cat}) a few studies do exist. Lancaster (Ref. 25), for example, estimated the cathode fall voltage for GMAW of steel as 15 V for a 118-A current. This value was derived from Pintard's (Ref. 26) measured voltage of *ca.* 19 V at an arc length of zero, along with the assumptions of a 2-V drop in both the electrode and the anode fall region. Other data of the cathode fall voltage, valid for arcs in general, are given by Guile (Ref. 27) as 10 to 20 V. Also, Vijh has calculated the cathode fall voltage for pure iron as 16.2 V (Ref. 28). This value agrees well with the experimental values of 17.1 to 18.0 V given by Grakov (Ref. 29), for current levels of 5 to 25 A.

Arc Power

The arc length determines the current and arc pressure distribution on the weld pool, which in turn determines the size and the shape of the weld fusion zone (Ref. 30). When the arc length is too short, the electrode can contact or short-circuit to the weld pool, which results in reduced base metal melting, a high, narrow weld deposit, variations in the heat input, and increased chances of forming weld defects. Excessive arc length causes a flat, shallow deposit, allows the arc to wander and increases spatter, and may cause porosity from air aspirated into the shielding gas.

The power P can be calculated using the expression

$$P = UI \quad (2)$$

where U is the voltage and I is the welding current.

The total process voltage U_{tot} can be expressed as

$$U_{tot} = U_{cont} + U_{elec} + U_{arc} \quad (3)$$

where U_{cont} is the voltage drop due to the contact resistance between the contact tube and the consumable electrode, U_{elec} is the voltage drop in the consumable electrode, and U_{arc} is the voltage drop in the arc. Because of the composite nature of the total process voltage, a measure of the true arc voltage alone cannot be obtained. Therefore, controlling the total process voltage does not ensure a constant arc length. Other work, however, has shown that arc radiation may be used to control the arc length (Refs. 31, 32).

The study of how arc radiation is related to arc geometry and welding parameters has been limited to the GTAW process (Refs. 33–35). Studies of the GMAW process have concentrated on the fraction of the total power that is input to the work (Refs. 36, 37). The fraction of power leaving the arc by radiation P_r in GTAW (Ref. 33) and other high current arcs (Refs. 38, 39) has been modelled as

$$Pr = \theta I U_{arc} \quad (4)$$

where θ is the fraction of arc power lost by radiation. An upper boundary for P_r can be calculated as the total power less the amount of power delivered to the workpiece. Using Ref. 36, the maximum P_r is 15% of the total power input to the process.

Even though Equation 4 was developed for GTAW, which does not include the complication of metal transfer across the arc, it can be applied to GMAW to obtain a measure of the power radiated by the arc.

Theoretical Modeling

The voltage drops in the arc column and in the electrode were calculated using a two-dimensional steady-state model and a one-dimensional steady-state model, respectively, as described in the following.

Calculation of the Voltage Drop in the Arc Column

A two-dimensional steady-state mathematical model has been developed to predict properties (for example: velocity, temperature, pressure, voltage) in the arc region of the GMAW process. In an earlier study, the model was applied to GMAW of aluminum in an argon atmosphere (Ref. 40). Calculated values for temperatures at a location halfway between the electrode and the workpiece differed by 0 to 6.1% for current values of 150 A and 0 to 3.8% for 250 A, in comparison with spectroscopically measured temperatures (Ref. 41). For this investigation, the model is applied to GMAW of mild steel.

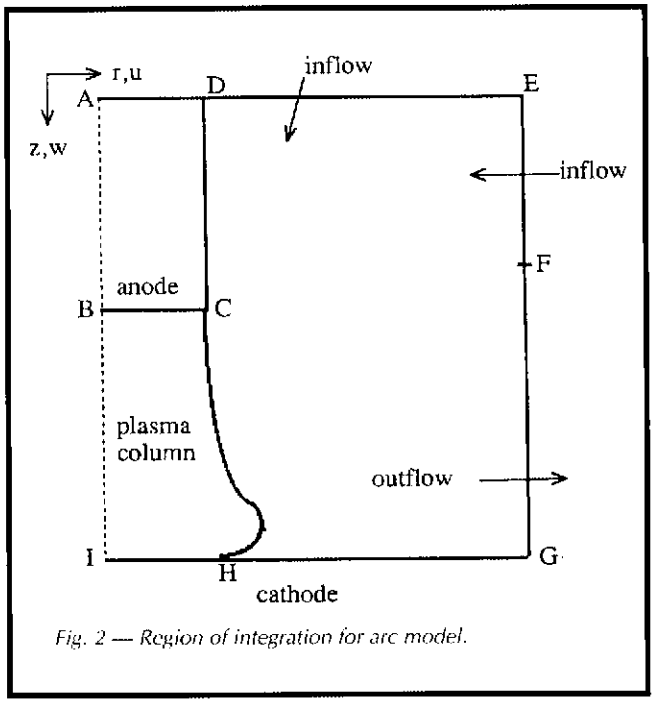

Fig. 2 — Region of integration for arc model.

The primary difference from the earlier model application to GMAW of aluminum (Ref. 40) is that the arc column is modeled under the assumption of local thermal equilibrium (LTE). Thus, the simplified approach to account for non-LTE conditions in the anode and cathode fall regions (through source terms in the plasma region close to the anode and cathode) is not used. The purpose of this approach is to focus on modeling the electric characteristics taking place in thermal equilibrium. As a result, the equilibrium voltage drop in the arc column can be calculated more accurately. The anode and cathode fall voltage are estimated by the combined theoretical and experimental approach used in this study.

The following paragraphs summarize the important assumptions, equations, and boundary conditions used in the model. A more detailed description of the mathematical model can be found in an earlier publication (Ref.40).

Mathematical Formulation

The outline of the computational domain for the welding arc is shown in Fig. 2, and the variables used in the figure are defined in the Appendix and Table 1. The system is assumed to be axisymmetric and steady. The gas flow is assumed to be laminar. This can be justified in a similar way used by McKelliget and Szekely for a GTAW system on the basis of laminar-turbulent transition of a free jet (Ref. 42). The plasma is assumed to be pure argon at atmospheric pressure, although the calculations are simulating experiments where a 95% argon - 5% carbon dioxide gas mixture is used. This assumption is necessary due to the lack of high-temperature thermophysical data for this gas mixture. The validity of this assumption is probably good, since additions of 5% oxygen (which is also an oxidizing reagent as carbon dioxide) to an argon plasma were found to have a negligible

Table 1 — Boundary Conditions for the Arc

Fig. 2	u	w	h, T(K)	Φ
BC, CD, AD	0	0	1810	0 (AD)
DE	0	$\frac{\partial \rho w}{\partial z} = 0$	300	$\frac{\partial \Phi}{\partial z} = 0$
EF, FG	$\frac{\partial \rho u}{\partial r} = 0$	$\frac{\partial w}{\partial r} = 0$	300 (inflow) $\frac{\partial h}{\partial r} = 0$(outflow)	$\frac{\partial \Phi}{\partial r} = 0$
IH	0	0	1810	$J_c = \frac{I}{\pi R_c^2}$
HG	0	0	1000	0

Integration domain shown in Fig. 2.

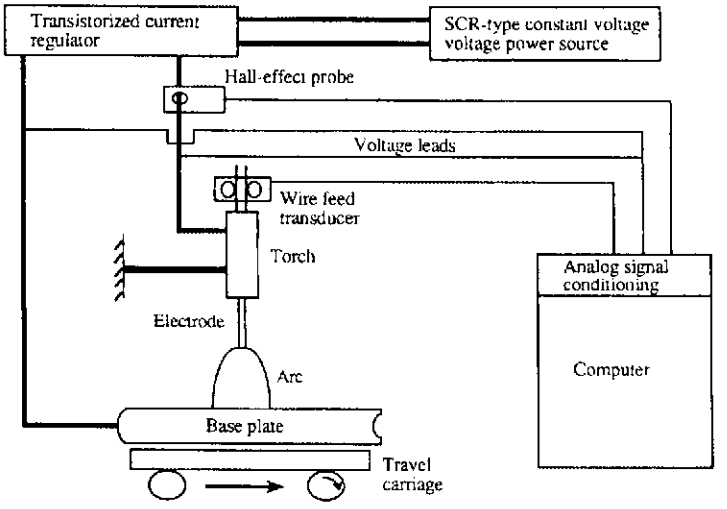

Fig. 3 — Outline of the welding equipment.

effect on the calculated arc parameters (Ref. 43). Also, the plasma is assumed to be in local thermal equilibrium (LTE) (*i.e.*, the electron and heavy particle temperatures are very similar). Hsu and coworkers (Refs. 44, 45) showed that this assumption is accurate through most of a gas tungsten arc, except near the anode and cathode surfaces and in the fringes. The plasma is optically thin so that radiation may be accounted for by using an optically thin radiation loss per unit volume. The influence of metal droplets is neglected. The consumable electrode is assumed to be cylindrical. Finally, the tip of the electrode and the workpiece surfaces are assumed to be flat.

In applying these assumptions, the equations (written in cylindrical coordinates) that need to be solved are conservation of mass, radial and axial momentum, thermal energy, and charge continuity (expressed in the form of the electrical potential). The definition of the electric potential is used to calculate the current densities, and Ampere's law is used to obtain the self-induced magnetic field.

The boundary conditions for the welding arc are listed in Table 1, and the variables used in Table 1 are defined in the Appendix. In the anode region (BC, CD in Fig. 2) a no-slip condition is used for the momentum boundary conditions. A no-slip condition means that the axial and radial plasma velocities very close to the anode and the cathode are very small (zero). The anode's enthalpy was calculated by considering a value corresponding to the melting temperature of pure iron, 1810 K. The equation for the conservation of charge continuity is the only equation to be solved within the electrode region, and therefore, the electric potential is set to be constant in region DA — Fig. 2. In region DE, a zero mass flow gradient $\partial pw/\partial z$ was postulated, together with an inlet enthalpy corresponding to a temperature of 300 K. Since it is not clear where inflow EF and outflow FG will take place in the fringes of the arc column, zero radial mass flow $\partial(\rho u)/\partial r$ and zero electric potential $\partial\Phi/\partial r$ gradients were specified.

Furthermore, the enthalpy is assumed to correspond to a temperature of 300 K for the gas entrained into the system, and the enthalpy gradient $\partial h/\partial r$ is assumed to be zero for mass flowing out of the system. Finally, in the cathode region GHI, a no-slip condition is used for the momentum equations. The cathode surface enthalpies within and outside the weld pool (cathode spot) region are taken at temperature values of 1810 and 1000 K, respectively. Here, an average value of the cathode spot radius R_c, representing the movement of the cathode spot, is chosen as 2.7 mm. Constant values of the current density I_c are used within and outside the cathode spot region:

$$J_c = \frac{I}{\pi R_c^2} \qquad r \le R_c \tag{5}$$

$$J_c = 0 \qquad r > R_c \tag{6}$$

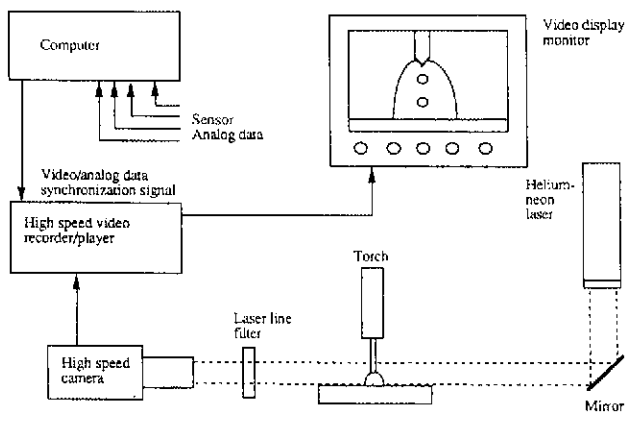

Fig. 4 — The image processing system.

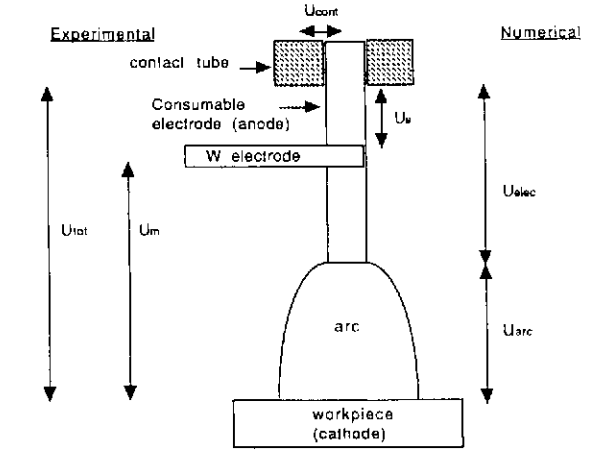

Fig. 5 — Outline of experimentally measured and numerically calculated voltage drops. The methods of evaluation of the voltage drops are given in Table 2.

Method of Solution

The solution of the governing equations and boundary conditions is obtained by using a modified version of 2EFIX, a two-dimensional steady-state code based on a finite volume scheme (Ref. 46). The difference equations are solved by iteration until the residuals are less than 1%. The current balance is satisfied within 1% for all calculations.

Experimental input to the model consists of current, arc length L_a, contact tube-to-workpiece distance C_{wd}, and electrode diameter d. Theoretical input in the form of thermophysical gas properties are taken from the publications by Liu (Ref. 47), Devoto (Ref. 48) and Evans and Tankin (Ref. 49). The value of the electrical conductivity of iron at its melting point is taken from a publication by Touloukian (Ref. 50).

Calculation of the Voltage Drop in the Consumable Electrode

A one-dimensional heat transfer model of the melting electrode is used to predict the voltage drop in the electrode. The same model has also been used to predict the electrode extension in an earlier publication (Ref. 51). The model of the electrode accounts for the following heat transfer processes: Joule heating in the electrode, heat absorption due to electrons condensing at the tip of the electrode, and heat transferred from the droplet together with conduction in the electrode. The electrical resistivity and the other thermophysical properties of the electrode were allowed to vary with temperature. Also, an unknown constant, representing the fraction of electrons that directly condense on the solid electrode and not on the droplet, is included in the model. This constant was experimentally determined for the spray transfer region by minimizing the error between the measured and the calculated value of the electrode extension (Ref. 51). The heat transfer model also predicted the steady-state temperature profile in the electrode, and the local resistivity was calculated using the data in Ref. 50. Finally, the voltage drop in the electrode was calculated as the integral of the resistivity multiplied by the current density.

Experimental Work

Welding equipment

As shown in Fig. 3, the welding equipment consists of a conventional constant voltage power source (650-A, silicon-controlled rectifier with an open circuit voltage of 54 V), a wire feeder, and a straight-body machine torch. The output of the power source is controlled by a series-linear regulator to provide smooth welding power. The current regulator has a flat frequency response to 3 kHz and when run in constant current mode has a nearly infinite current-voltage slope. The torch is held stationary, while the base plate is moved by a motorized travel carriage.

Table 2 — Voltage Contributions in GMAW System

	Voltage Drop	Method of Evaluation	Table
$U_{an}+U_{cat}$	Sum of anode and cathode fall regions (non-LTE)	Derived using Equation 8	6
U_{arc}	In arc	Derived using Equation 3	6
U_{col}	In arc column	Calculated with 2-D model	6
U_{cont}	Due to contact resistance between contact tube and electrode	Derived using Equation 7	5
U_e	In electrode: between contact tube and tungsten probe	Calculated with 1-D model	5
U_{elec}	In electrode	Calculated with 1-D model	6
U_m	Between tungsten probe and workpiece	Measured	5
U_{tot}	Between contact tube and workpiece	Measured	3

Some shown in Fig. 5.

Table 3 — Measured Values of Current, Voltage and Wire Feed Speed

Exp. No.	I (A)	U_{tot} (V)	V_w (m/s)
1	201.9 (0.83)[a]	28.390 (0.91)[a]	0.0928 (0.0026)[a]
2	224.3 (0.67)	29.046 (0.65)	0.1089 (0.0028)
3	250.3 (0.61)	28.959 (0.74)	0.1222 (0.0034)
4	275.4 (0.49)	29.253 (0.36)	0.1346 (0.0037)
5	298.4 (0.56)	30.281 (0.46)	0.1536 (0.0039)
6	326.2 (0.53)	30.796 (0.39)	0.1650 (0.0042)

(a) Standard deviation.

Instrumentation

A high-speed video camera and a laser illumination system were used to obtain images of the contact tube, electrode, and weld pool surface, as is illustrated in Fig. 4. Instantaneous values for the electrode extension, arc length, and contact-tube-to-work distance were measured automatically frame by frame from videotapes of the welds using an image processor. More specifically, the image processor was used to detect the outline of the electrode and its location relative to the weld pool surface.

A Hall-effect transducer located in the welding circuit (Fig. 3) measured current. An optical encoder driven by pinch rollers measured electrode feed rate. Total process voltage was measured between the contact tube and the workpiece. The drop between the contact tube and the electrode was obtained by measuring the voltage between the contact tube and a 1.5-mm-diameter tungsten wire in sliding contact with the electrode, as shown in Fig. 5.

Filtered signals from the current, voltage and wire feed speed were sampled by a computer equipped with a multichannel analog-to-digital converter, and sensor data were synchronized with the video system data.

Experimental Procedure

Welds were made on low-carbon steel plates using a 1.14-mm-diameter ER100S-1 (low carbon, uncoated) electrode with a shielding gas of 95% argon - 5% carbon dioxide, a nominally 19-mm (0.75-in.) contact-tube-to-workpiece distance, and a constant current. As defined in Ref. 52, the cast of an electrode is the diameter that one loop of unrestrained electrode assumes. When the unrestrained loop of electrode is placed on a horizontal surface, the helix is the vertical distance the end of the electrode is above the surface. Here, the cast of the electrode varied from about 760 mm (30 in.) for electrode taken near the outside of the spool to about 660 mm (26 in.) for electrode taken near the inside. The helix of the electrode varied from about 6 mm for the electrode taken near the outside of the spool to about 30 mm (1.2 in.) for

Table 4 — Results from Image Analysis

Exp. No.	L_a (mm)	E_e (mm)	C_{wd} (mm)
1	8.49	10.30	18.79
2	8.12	11.39	19.51
3	7.26	11.63	18.89
4	6.83	11.00	17.83
5	7.15	12.07	19.22
6	8.26	10.13	18.39

wire taken near the inside. Workpiece travel speed was set from 4.6 to 7.3 mm/s (11 to 17. in./min) depending on the welding current. The inside diameter of the contact tube was 1.37 mm (0.05 in.), and the tube was 35.0 mm (1.4 in.) long.

Sensor data were collected at 1000 samples per second, and video data were taken at 1000 frames per second. For each welding condition, 15 sets of data, each lasting 0.2 s, were recorded.

Results and Discussion

Voltage Characteristics

In order to study the voltage distribution in GMAW, a total of six experimental runs were carried out using the spray mode. The different voltage contributions and the methods of evaluation are given in Table 2. Figure 5 shows how some of the separate voltage contributions are derived experimentally and numerically. The current and arc length ranges are 202 to 326 A and 10 to 12 mm (0.4 to 0.48 in.), respectively. Measured data and the standard deviation of current, total process voltage, and wire feed speed are given in Table 3. The values of arc length, electrode extension E_e and contact-tube-to-work distance are listed in Table 4.

Table 5 — Derivation of Voltage Drop Due to Contact Resistance (U_{cont})

Exp. No.	U_m (V)	U_e (V)	U_{cont} (V)
1	26.940 (1.07)[a]	0.087	1.363
2	27.516 (0.83)	0.096	1.434
3	27.154 (0.87)	0.126	1.679
4	27.338 (0.43)	0.145	1.770
5	28.397 (0.46)	0.167	1.717
6	28.883 (0.43)	0.179	1.734

(a) Standard deviation.

U_{elec}

As mentioned earlier, the voltage drop in the electrode U_{elec} is calculated using the one-dimensional model. The voltage drop in the consumable electrode is shown as a function of axial distance from the contact tube in Fig. 6. Here, U_{elec} ranges from 0.46 to 1.12 V for the studied range of currents. Specific data on the calculated voltage drops in the electrode for all experiments are summarized in Table 6. Our calculations of the voltage drops in the electrode are lower than the 4 to 5 V reported by Waszink and van den Heuvel (Ref. 8). However, in their experiments, the electrode extensions were approximately three times longer than the measured electrode extensions in our study. A longer electrode extension increases the electrical resistance of the electrode, so the voltage drop in the electrode is larger. This is due to the fact that the voltage is derived as the integral of the resistivity multiplied by the current density. Therefore, the measured values of U_{elec} by Waszink and van den Heuvel (Ref. 8) are higher than the corresponding values in our study.

U_{elec} calculations from the one-dimensional model are also compared with results from Equation 1 (derived by Halmøy, Ref. 7) in Fig. 7. Here, the parameters H_m and φ in Equation 1 are taken as 11.1×10^9 J/m^3 and 3.5 V, respectively (Ref. 7). The current density in Equation 1 is calculated from Equation 5, using an electrode of radius 0.57 mm and currents from Table 3. Figure 7 shows a similar dependence of the voltage drop in the electrode on the current from the one-dimensional model and the results derived using Equation 1. However, the results calculated using Equation 1 are about 1 to 1.5 V higher than the results from the one-dimensional model. One explanation could be the somewhat low value of the work function of iron of 3.5 V used in Equation 1, as recommended by Halmøy (Ref. 7). Michaelson (Ref. 53) reported that the work function for iron is 4.5 V. Substituting this value into Equation 1 results in a 1 V decrease of the voltage in the electrode and gives fair agreement (19% to 55%) with the derived value of U_{elec} using our one-dimensional model.

U_{cont}

The voltage drop due to the contact resistance between the contact tube and the consumable electrode (U_{cont}) is derived from the expression

$$U_{cont} = U_{tot} - U_m - U_e \qquad (7)$$

where U_m is the voltage measured between the tungsten probe and the workpiece, and U_e is the calculated (Table 2) voltage drop in the electrode between the contact tube and the tungsten probe, as shown in Fig. 5. The values of U_m and U_e are given in Table 5, along with data derived for U_{cont}. The voltage drops due to the contact resistance are in the range

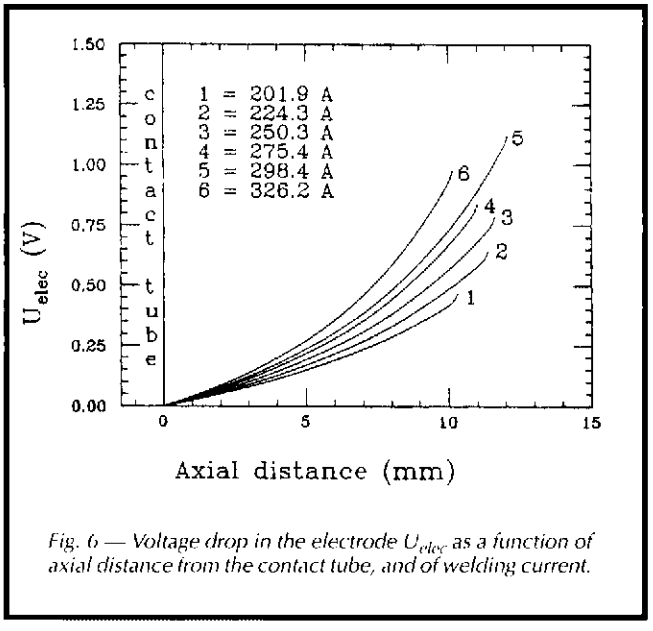

Fig. 6 — Voltage drop in the electrode U_{elec} as a function of axial distance from the contact tube, and of welding current.

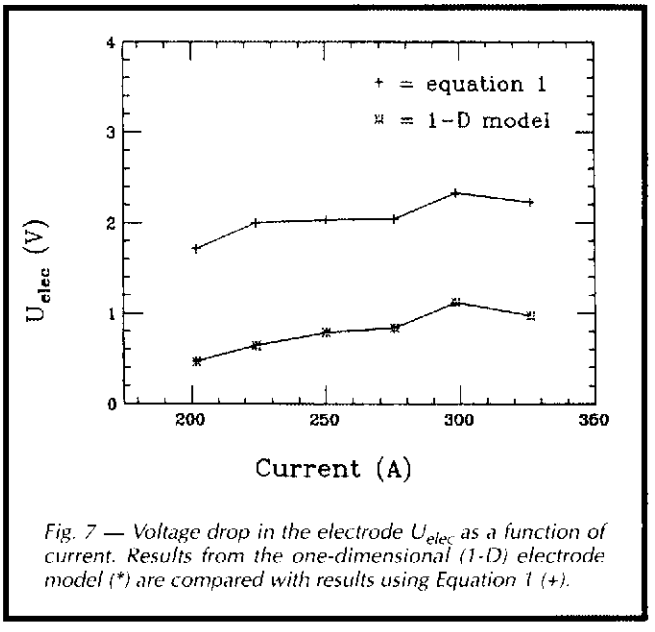

Fig. 7 — Voltage drop in the electrode U_{elec} as a function of current. Results from the one-dimensional (1-D) electrode model (*) are compared with results using Equation 1 (+).

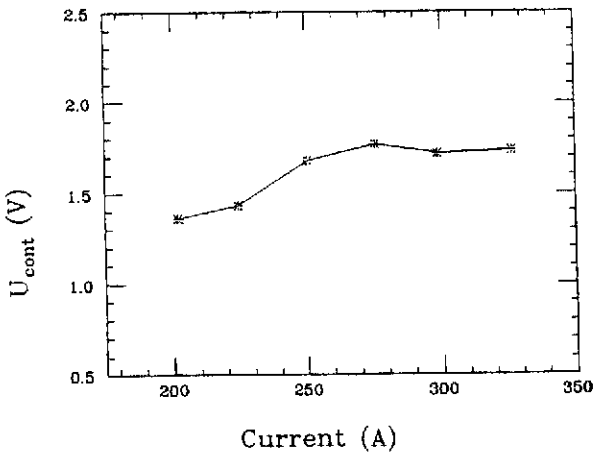

Fig. 8 — Voltage drop due to the contact resistance between the contact tube and the electrode U_{cont} as a function of welding current.

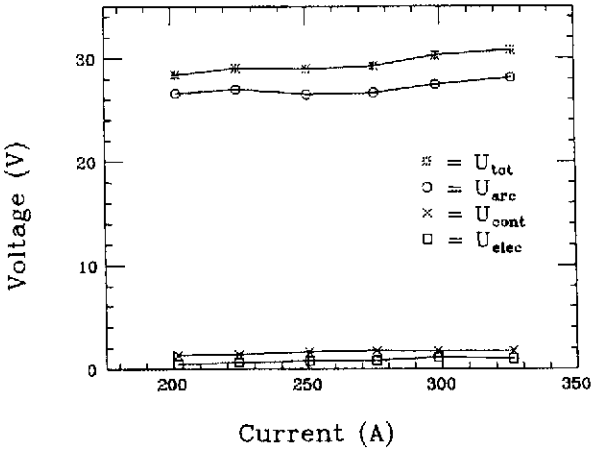

Fig. 9 — U_{tot}, U_{arc}, U_{elec} and U_{cont} as a function of welding current.

of 1.36 to 1.77 V, as shown in Fig. 8. These results are greater than the values of 0.3 to 0.6 V for stainless steel reported by Waszink and van den Heuvel (Ref. 8).

U_{arc}

Knowing U_{tot}, U_{elec}, and U_{cont}, we can calculate the voltage drop in the arc using Equation 3. The calculated values of U_{arc} are shown in Table 6 and plotted with the data on U_{elec}, U_{cont}, and U_{tot} in Fig. 9. The dominant voltage drop in the GMAW system occurs in the arc region.

The voltage distribution in the arc between the consumable electrode (anode) and the workpiece (cathode) can be divided into three main regions, the anode fall U_{an}, the arc column U_{col}, and the cathode fall U_{cat}:

$$U_{arc} = U_{an} + U_{col} + U_{cat} \quad (8)$$

The calculated arc column (Table 2) is in local thermal equilibrium, and the electric field strength (voltage gradient), as illustrated in Fig. 10, is relatively uniform. Figure 10 shows the electric field strength to be about –1 V/mm. However, the absolute value of the electric field strength significantly increases in the arc regions close to the anode and the cathode. This has also been observed for gas tungsten arcs (Refs. 23, 24).

As mentioned earlier, the voltage drop in the arc column is calculated by the two-dimensional arc model (Table 2). It is shown as a function of welding current in Figure 11, while the calculated specific

Table 6 — Voltage Drops

Exp. No.	U_{elec} (V)	U_{arc} (V)	U_{col} (V)	$U_{an} + U_{cat}$ (V)
1	0.465	26.56	11.63	14.93
2	0.645	26.97	12.09	14.88
3	0.787	26.49	12.16	14.33
4	0.837	26.65	12.56	14.09
5	1.120	27.44	13.38	14.06
6	0.974	28.09	14.77	13.32

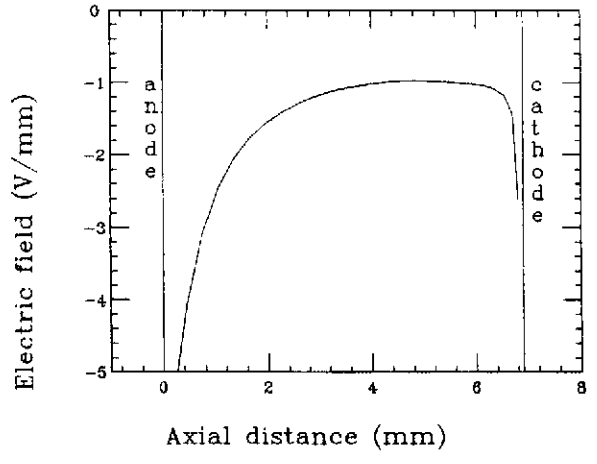

Fig. 10 — Electric field intensity in the arc column vs. the axial distance from the contact tube. The current and arc length are 274.4 A and 6.9 mm, respectively.

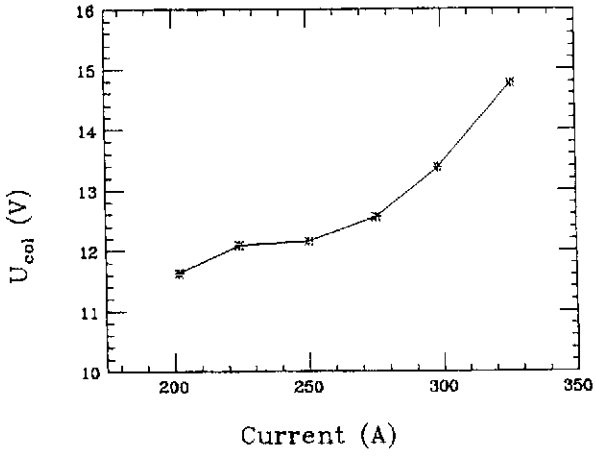

Fig. 11 — Voltage drop in the arc column U_{col} as a function of welding current.

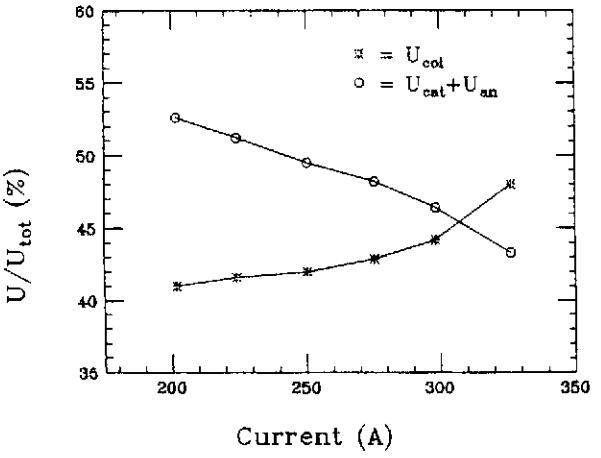

Fig. 12 — Percentage of the voltage drop in the anode and cathode fall regions $U_{cat} + U_{an}$ and the arc column U_{col} relative to the total process voltage U_{tot}, as a function of the welding current.

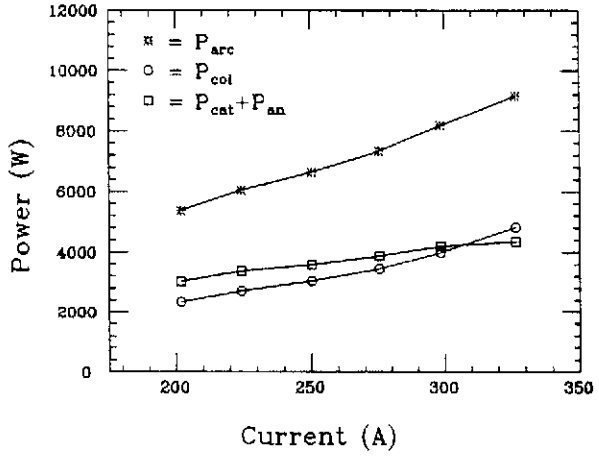

Fig. 13 — Total power in the arc P_{arc}, power in the arc column P_{col}, and sum of power in the anode and cathode fall regions $P_{an} + P_{cat}$, as a function of the welding current.

values of U_{col} for each experiment are given in Table 6. The voltage in the arc column increases with an increased welding current, especially at currents above 250 A.

$U_{an} + U_{cat}$

The sum of the voltage drops in the cathode and anode fall regions (non-LTE regions) $U_{an} + U_{cat}$ is calculated from Equation 8 using U_{arc} as derived from Equation 3 and U_{col} as calculated with the two-dimensional arc model — Table 6. The percentage of the total voltage drop in the anode and cathode fall regions relative to U_{tot} is plotted in Fig. 12 along with the corresponding percentage of U_{col} relative to U_{tot}, as a function of the welding current. Below current values of about 307 A, the combined voltage drops of the anode and cathode fall regions dominate. Furthermore, while the percentage of voltage drop in the arc column increases with an increased current, the percentage of the voltage drop in the anode and cathode fall regions decreases with an increased current. The decrease of the voltage drop in an anode fall region with an increased current has been reported previously (Ref. 15).

The sum of the voltage drops in the anode and cathode fall regions varies from 13.32 to 14.93 V, as shown in Table 6. Most of this total voltage drop takes place in the cathode region, since energy needs to be supplied to the metal cathode in order to emit the electrons. A smaller voltage drop probably occurs at the anode, since the electrons condense on the anode and, in turn, release energy. Moreover, a comparison of our results with the theoretical value of the cathode fall voltage of 16.2 V by Vijh (Ref. 28) indicates that the anode fall voltage is indeed very small. It might even be negative, as Pfender and coworkers (Refs. 17, 18) reported for gas tungsten arcs.

The derived voltage drops representing the non-LTE regions of 13.32 to 14.93 V are also lower than the experimental cathode fall values of 17.1 to 18.0 V reported by Grakov (Ref. 29). Our derived voltage drops of the anode and cathode fall regions are also lower than the experimental voltage at zero arc length of 19 V, as measured by Pintard (Ref. 26). Pintard's measurements included the voltage drop in the electrode. Even if we subtract a 1.5 to 2 V contribution of U_{elec}

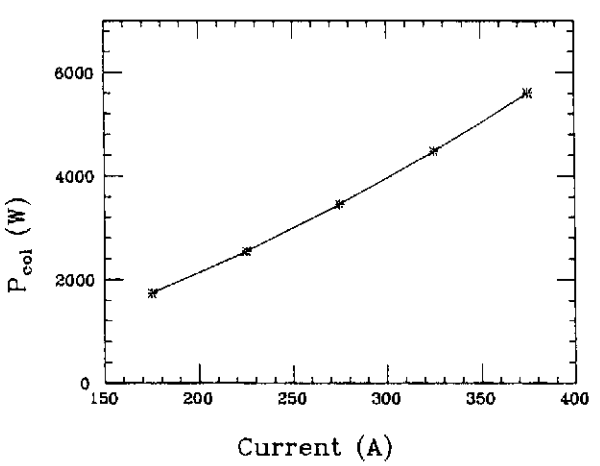

Fig. 14 — Power in the arc column P_{col} as a function of welding current. The arc length is 6.9 mm.

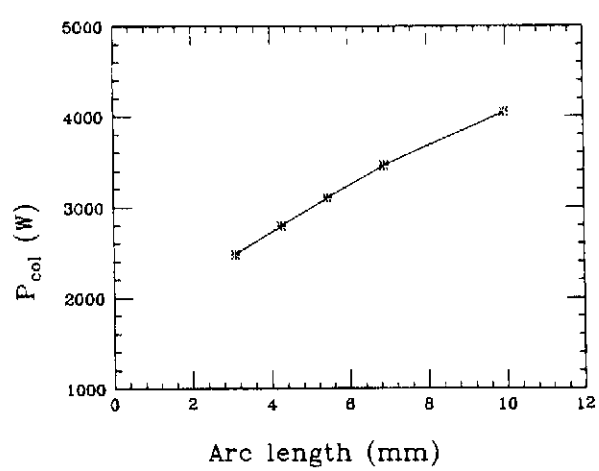

Fig. 15 — Power in the arc column P_{col} vs. arc length. The current is 275 A.

from Pintard's result, our derived values of the voltage in the non-LTE regions are lower than Pintard's measurements. However, Pintard's and Grakow's experiments were done using current values of 118 A and of 5 to 25 A, respectively. These currents are lower than the range of currents of 201.9 to 326.2 A that are used in this study. Figure 12 shows that the sum of the voltage drop in the anode and the cathode fall regions decreases with an increasing current. Therefore, it is understandable that our results of the sum of the anode and cathode fall voltages could be lower than the data that have been reported by Pintard (Ref. 26) and Grakov (Ref. 29).

Power Characteristics

The power characteristics in the arc, calculated using Equation 2, are illustrated in Fig. 13. Data for the current and arc voltage are taken from Tables 3 and 6. The figure shows that the total power in the arc increases with an increasing current. The sum of the power in the anode and cathode fall regions increases more slowly with increased current than does the power in the arc column. However, the sum of the powers in the anode and cathode fall regions is higher than the power in the arc column for currents lower than about 307A.

The variation of the experimental arc lengths of 10.1 to 12.1 mm (Table 4) is believed to affect the derived power characteristics. Therefore, a series of calculations was performed (using the two-dimensional arc model) to study the separate dependence of the power in the arc column on welding current and arc length. Figure 14 shows that the power in the arc column increases with increased current at a constant arc length of 6.9 mm. Also, Fig. 15 shows that the power in the arc column increases with an increased arc length at a constant current of 275 A.

As shown in Fig. 16, the power input affects the melting and tapering of the electrode, as well as the formation and detachment of the droplets from the electrode. As a result the power input also affects the size and frequency of the droplets, and the solidification of the weld pool, along with the resulting microstructure and mechanical properties of the weld. Since the power varies with both arc length and current, it is critical to control these parameters in order to sustain a constant input of power to the system.

As indicated in Figs. 14 and 15, the power in the arc column increases with increasing currents and arc lengths. Based upon Equations 2 and 4, the fraction of power leaving the arc by radiation also increases with increasing currents and arc lengths. The radiative power (arc light intensity) can be measured with a photodiode. Madigan and Quinn (Ref. 32) showed that measurements of arc current and arc light intensity can be used to measure arc length, for the specific shielding gas and electrode composition used during those experiments.

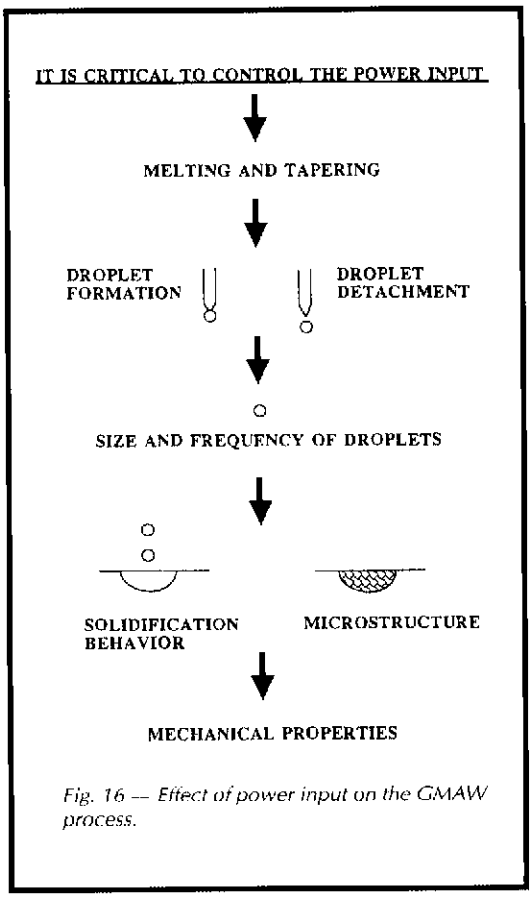

Fig. 16 — Effect of power input on the GMAW process.

Conclusions

The most significant findings of this study can be summarized as:

1) Voltage characteristics: A dominant voltage drop takes place in the arc region. In the arc region, the voltage drop in the non-LTE regions decreased with increasing current and dominated the voltage drop for currents below about 307 A. The voltage drop in the arc column increased with increasing current and became the dominating voltage drop in the arc for currents exceeding about 307 A. Small voltage drops occurred in the electrode and in the region of contact between the contact tube and the electrode.

2) Power characteristics: Arc power increased with increasing current. Similar to the results for the voltage distribution in the arc, the dominating contributions of the power occurred in the anode and cathode fall regions for currents below about 307 A. A numerical study showed that the power characteristics in the arc increase both with increasing arc length and increasing current. From these results we conclude that it is critical to control the arc length in order to control the power in the arc, while welding in the constant current mode.

References

1. American Welding Society. 1991. *Welding Handbook* pp. 109–113, Miami, Florida.

2. Eagar, T. W. 1990. An iconoclast's view of the physics of welding — rethinking old ideas. *Recent Trends in Welding Research*, eds. S. A. David and J. M. Vitek, pp. 1–6, ASM International, Materials Park, Ohio.

3. Cobine, J. D., and Burger, E. E. 1955. Analysis of electrode phenomena in the high-current arc. *J Appl. Phys.* 26(7): 895–900.

4. Quigley, M. B. C., Richards, P. H., Swift-Hook, D. T., and Gick, A. E. F. 1973. Heat flow to the workpiece from a TIG welding arc. *J. Phys. D : Appl. Phys.* 6: 2250–2258.

5. Jackson, C. E. 1960. The science of arc welding: Part II - Consumable electrode welding. *Welding Journal* 39(5): 177-s to 190-s.

6. Halmøy E. 1986. Electrode wire heating in terms of welding parameters. *The Physics of Welding* ed. J. F. Lancaster, pp. 154–155 and 330–336, Oxford, Pergamon Press.

7. Halmøy, E. 1990. Current-voltage process characteristics in GMAW. International Institute of Welding, Doc. 212-773-90.

8. Waszink, J. H., and van den Heuvel, G. J. P. M. 1979. Measurements and calculations of the resistance of the wire extension in arc welding. *Int. Conf. Arc Physics and Weld Pool Behavior* pp. 227–239, London, The Welding Institute.

9. Schoeck, P. A. 1963. An investigation of the anode energy balance of high intensity arcs in argon. *Modern Developments in Heat Transfer*, ed. W. Ibele, pp 363–364, New York, Academic Press.

10. Finkelnburg, W., and Segal, S.M. 1951. The potential field in and around a gas discharge, and its influence on the discharge mechanism. *Phys. Rew.* 83(3): 582-585.

11. Block, Von M. J., and Finkelnburg, W. 1953. Über die axiale ausdehnung des anodenfallgebiets beim kohlelichtbogen. *Z. Naturforsch* 8A: 758.

12. Busz-Peuckert, G. and Finkelburg, W. 1955. Die abhängigkeit des anodenfalles von stromstarke und bogenlänge bei hochtemperaturbögen. *Z. fur Physik.* 140: 540–546.

13. Busz-Peuckert, G., and Finkelnburg, W. 1956. Zum anodenmechanismus des thermischen argonbogens. *Z. für Physik.* 144: 244–251.

14. Dickson, D. J., and von Engel, A. 1967. Resolving the electrode fall spaces of electric arcs. *Proc. Roy. Soc.* 300: 316–325.

15. Wilkinson, J. B., and Milner, D. R.

1960. Heat transfer from arcs. *Brit. Weld. J.* 2: 115–128.

16. Guile, A. E. 1986. The electric arc. *The Physics of Welding*, ed. J. F. Lancaster, pp. 120–145, Oxford, Pergamon Press.

17. Dinulescu, H. A., and Pfender, E. 1980. Analysis of the anode boundary layer of high intensity arcs. *J. Appl. Phys.* 51(6): 3149–3157.

18. Sanders, N. A., and Pfender, E. 1984. Measurements of anode falls and anode heat transfer in atmospheric pressure high intensity arcs. *J. Appl. Phys.* 55(3): 714–722.

19. Hsu and Pfender. 1983. Analysis of the cathode region of a free-burning high intensity argon arc. *J. Appl. Phys.* 54: 3818–3824.

20. Delalondre, C., and Simonin, O. 1990. Modelling of high intensity arcs including a non-equilibrium description of the cathode sheath. *Colloque de Physique* 51: C5-199-206.

21. Zhu, P., Lowke, J. J., and Morrow, R. 1992. A unified theory of free burning arcs, cathode sheaths and cathodes. *J. Phys. D : Appl. Phys.* 25: 1221–1230.

22. Guile, A. E. 1971. Arc-electrode phenomena. *Proc. IEE, IEE REV.* 118(9R): 1131–1154.

23. Essers, W. G., and Walter, R. 1980. Some aspects of the penetration mechanisms in metal-inert-gas (MIG) welding. *Int. Conf. Arc Physics and Weld Pool Behavior* pp. 289–300, London, The Welding Institute.

24. Lancaster, J. F. 1987. The physics of fusion welding; Part 1 : The electric arc in welding. *IEE Proc.* 134(5): 233–252.

25. Lancaster, J. F. 1986. Metal transfer and mass flow in the weld pool. *The Physics of Welding*, ed. J. F. Lancaster, pp. 228–305, Oxford, Pergamon Press.

26. Pintard, J. 1962. Some experimental data on short-circuit transfer. *Physics of the Welding Arc* pp. 92–97, London, The Institute of Welding.

27. Guile, A. E. 1970. Studies of short electric arcs in transverse magnetic fields with application to arc welding. *Welding in the World* 8(1):43–53.

28. Vijh, A. K. 1976. The improved electrochemical theory for the quantitative estimation of the magnitudes of cathode fall voltages in pure metal arcs. *J. de Chim. Phys.* 73(5): 566–568.

29. Grakov, V. E. 1967. Cathode fall of an arc discharge in a pure metal I. *Sov. Phys. - Techn. Phys.* 12(2): 286–292.

30. American Welding Society. 1991. *Welding Handbook* Vol. 2, pp. 110–155, Miami, Fla.

31. Johnson, C. A., and Sciaky, A. M. 1966. System for controlling arc length of welding arcs. U.S. Patent 3236997.

32. Madigan, R. B., and Quinn, T. P. 1992. Sensing droplet detachment and electrode extension for control of gas metal arc welding. *Conf. Proc. 3rd ASM Int. Trends in Welding Research.* pp. 999–1002, ASM International, Materials Park, Ohio.

33. Ghent, H. W., Roberts, D. W., Hermance, C. E., Kerr, H. W., and Strong, A. B. 1979. Arc efficiences in TIG welds. *Arc Physics and Weld Pool Behavior*, pp. 17–23, London, The Welding Institute.

34. Allum, C. J. 1983. Power dissipation in the column of a TIG welding arc. *J. Phys. D: Appl. Phys.* 16: 2149–2165.

35. Doam, R. T., and Drew, P. N. 1989. *Conf. Proc. of Advances in Joining and Cutting Processes*, London, The Welding Institute.

36. Watkins, A. D., Smartt, H. B., and Einerson, C. J. 1989. *Proceedings of the 2nd International Conference on Trends in Welding Research* pp. 19–23, ASM International, Materials Park, Ohio.

37. Essers, W. G., and Walter, R. 1989. Heat transfer and penetration mechanisms with GMA and plasma-GMA welding. *Welding Journal* 60(1): 37-s to 42-s.

38. Strachan, D. C., Lidgate, D., and Jones, G. R. 1977. Radiative energy losses from a high-current air-blast arc. *J. Appl. Phys.* 48(6): 2324–2330.

39. Malghan, V. R., Fang, M. T. C., and Jones, G. R. 1977. Investigation of quasi steady-state high-current arcs in an orifice air flow. *J. Appl. Phys.* 48(6): 2331–2337.

40. Jönsson, P. G.,Westhoff, R. C., and Szekely, J. 1992. Arc characteristics in gas metal arc welding. *J. of Appl. Phys.* 74(10): 5997–6006.

41. Smårs, E. A., and Acinger, K. 1968. Material transport and temperature distribution in arc between melting aluminum electrodes. International Institute of Welding, Doc. 212-162-68.

42. McKelliget, J., and Szekely, J. 1986. Heat transfer and fluid flow in the welding arc. *Met. Trans.* A 17(7): 1139–1148.

43. Jönsson, P. G. 1993. Arc parameters and metal transfer in gas metal arc welding. Sc.D. dissertation. Massachusetts Institute of Technology, Cambridge, Mass.

44. Hsu, K. C., Etemadi, K., and Pfender, E. 1983. Study of the free-burning high intensity argon arc. *J. Appl. Phys.* 54(3): 1293–1301.

45. Hsu, K. C., and Pfender, E. 1983. Two-temperature modeling of the free burning arcs in argon. *J. Appl. Phys.* 54: 4359–4366.

46. Pun, W. M., and Spalding, D. B. 1976. Rep. No. HTS/76/2. Heat Transfer Section, London, Imperial College.

47. Liu, C. F. 1977. Numerical analysis of the anode region of high intensity. Ph.D. dissertation. University of Minnesota, Minneapolis, Minn.

48. Devoto, R. S. 1973. Transport coefficients of ionized argon. *Phys. of Fluids* 16(5): 616–623.

49. Evans, D. L., and Tankin, R. S. 1967. Measurement of emission and absorption of radiation by an argon plasma. *Phys. of Fluids* 10(6): 1137–1144.

50. Touloukian, Y. S. 1967. *The Elements, Thermophysical Properties of High Temperature Solid Materials*, p. 581, Macmillan, New York, N.Y.

51. Quinn, T. P., Madigan, R. B., and Siewert, T. A. 1992. An electrode extension model for gas metal arc welding. *Welding Journal* 73(10): 241-s.

52. American Welding Society. 1979. *Specification for Low Alloy Steel Filler Metals for Gas Shielded Arc Welding*, p. 10, ANSI/AWS Standard, A5.28-79, Miami, Fla.

53. Michaelson, H. B. 1977. The work function of the elements and its periodicity. *J. Appl. Phys.* 48(11):4729–4733.

54. Lancaster, J. F. 1986. The electric arc in welding. *The Physics of Welding*, ed. J. F. Lancaster, pp. 151–153, Oxford, Pergamon Press.

Appendix

Nomenclature

C_{wd}	Contact-tube-to-workpiece distance (mm)
d	Electrode diameter (mm)
E_e	Electrode extension (mm)
h	Plasma enthalpy (J/kg)
H_m	Experimental constant representing the total heat input per unit volume of wire necessary to melt and detach the droplets (J/m^3)
I	Welding current (A)
J	Current density (A/m^2)
J_c	Cathode current density (A/m^2)
L_a	Arc length (mm)
P	Power(W)
P_{an}	Power in the anode fall region(W)
P_{arc}	Power in the arc (W)
P_{cat}	Power in the cathode fall region (W)
P_{col}	Power in the arc column (W)
P_r	Power leaving the arc by radiation (W)
r	Radial distance (m)
R_c	Cathode spot (weld pool) radius (m)
T	Temperature (K)
u	Radial velocity (m/s)
U	Voltage (V)
U_{an}	Voltage drop in the anode fall region (V)
U_{arc}	Voltage drop in the arc (V)
U_{cat}	Voltage drop in the cathode fall region (V)
U_{col}	Voltage drop in the arc column (V)
U_{cont}	Voltage drop due to contact resistance between contact tube and electrode (V)
U_e	Voltage drop in the electrode between the contact tube and the tungsten probe(V)
U_{elec}	Total voltage drop in the electrode (V)
U_m	Measured voltage between the tungsten probe and the workpiece (V)
U_{tot}	Measured voltage between the contact tube and the workpiece (V)
w	Axial velocity (m/s)
v_w	Wire feed speed (m/s)
z	Axial distance (m)

Greek symbols

ρ	Density (kg/m^3)
Φ	Electric potential (V)
φ	Work function (V)
θ	Fraction of arc power lost by radiation (-)